Department of Physics and Astronomy
University of Heidelberg

Bachelor Thesis in Physics
submitted by

Felix Artur Wiard Scherz

born in Stuttgart (Germany)

2018

Optimization of Physical Vapor Deposition for Yttrium

This bachelor thesis has been carried out by Felix Artur Wiard Scherz at the
Kirchoff-Institute for Physics in Heidelberg
under the supervision of
Prof. Dr. Laura Na Liu

Abstract

Yttrium exposed to hydrogen exhibits a reversible, metal-insulator phase transition, making it a very interesting material for nanostructure fabrication, as it allows for the modficiation of optical characteristics of the material, even after manufacturing.
This thesis concerns itself with the physical vapor deposition process of thin yttrium films (50 nm) that exhibit the desired phase transition characteristics when exposed to hydrogen. By optimization of evaporation parameters such as deposition rate and ambient pressure, as well as film geometry, a repeatable manufacturing method was developed, allowing for the deposition of phase transitioning yttrium films.

Zusammenfassung

Yttrium zeigt eine durch Wasserstoff induzierte Phasentransformation vom metallischen zum dielektrischen Zustand, ein Effekt der Yttrium zu einem interessanten Material für die Nanotechnologie macht, da es erlaubt, optische Eigenschaften auch nach der Herstellung noch zu beeinflussen.
Diese Arbeit behandelt die Herstellung dünner Yttriumfilme (50 nm) mittels Elektronenstrahlverdampfung. Durch Optimierung der Herstellungsparameter wie Beschichtungsrate und Filmgeometrie wurde eine Methode zur Herstellung aktiver Yttriumfilme entwickelt.

Contents

1 Introduction

One of the first experiments on the hydrogen induced phase transition was conducted by Huiberts et al. in 1997 [7] focusing on changes in electrical and optical properties of yttrium films when exposed to hydrogen. Of particular interest is the reversible part of the phase transition:

$$\mathrm{Y} \longrightarrow \mathrm{YH_2} \rightleftharpoons \mathrm{YH_3}$$

as the YH_3 phase is semiconducting, while the YH_2 phase has metallic properties. Due to the low mass of the hydrogen atom making for a fast diffusion process, this phase transition can be rapid, even at room temperature [18].
In the field of plasmonics, the use of such phase transition materials that change their optical properties during the transition allows for the construction of active optical nanodevices that can be manipulated using external stimuli [17].
A core problem with yttrium films is that it oxidizes rapidly when exposed to air. To overcome this problem, protective layers made up of platinum or palladium are used to not only prevent oxidation, but to act as a catalytic layer to split hydrogen molecules.
Within this work thin yttrium films with a protective palladium layer were produced using electron-beam physical vapor deposition. By variation of the deposition parameters the goal is to determine a reliable method of producing active yttrium films that exhibit a hydrogen induced phase change with the ultimate goal of using the method in the nanofabrication process.
Possible applications of yttrium in nanostructures include the realization of switchable plasmonics devices. Even a simple yttrium film can act as a hydrogen sensor through monitoring changes in transmittance.

After introducing basic principles of thin film evaporation (section 2.1) and the optical characteristics of thin films (section 2.2), section 2.3 gives a brief overview of the hydrogen induced phase transition of yttrium. In chapter 3 the experimental methods are presented, explaining the evaporation setup and the optical measurements that were used to observe the phase transition. Results for different films will be presented in chapter 4, followed by a discussion and a brief summary of the findings.

2 Theory

2.1 Thin Film Evaporation

The goal of thin film deposition is to transfer atoms from a heated source material onto a substrate to produce a thin film. This is achieved by increasing the temperature of the source material until sufficient evaporation is achieved. The following subsections will give an introduction into the evaporation process.
The vapor pressure for a given material describes the pressure exerted by the gaseous phase in thermodynamic equilibrium with its liquid phase at a given temperature. A connection between temperature T and vapor pressure p can be made starting with the Clausius-Clapeyron equation [10]:

$$\frac{\mathrm{d}p}{\mathrm{d}T} = \frac{\Delta H(T)}{T\Delta V} \tag{2.1}$$

where $\Delta H(T)$ and ΔV are the differences in enthalpy and volume between the vapor (v) and condensed phase (c). Assuming $V_\mathrm{v} \gg V_\mathrm{c}$ and the ideal gas model leads to the simplification $\Delta V \approx V_\mathrm{v} = RT/p$ with R being the ideal gas constant. With the approximation that the difference in enthalpy between the phases is given by the molar heat of evaporation ΔH_e, eq. 2.1 can be rewritten as:

$$\frac{\mathrm{d}p}{\mathrm{d}T} \approx \frac{p\Delta H_\mathrm{e}}{RT^2} \tag{2.2}$$

which through integration transforms to:

$$\ln p \approx -\frac{\Delta H_e}{RT} + C \Longrightarrow p = p_0 \exp\left(-\frac{\Delta H_\mathrm{e}}{RT}\right) \tag{2.3}$$

which is only valid in a narrow temperature range due to the approximations. For better accuracy the temperature dependence of $\Delta H(T)$ must be considered.
Vapor pressures for a range of temperatures for yttrium, palladium, titanium, and tungsten are shown in fig. 2.1. Over a greater temperature range, where the enthalpy change becomes temperature dependent, the vapor pressure can be expressed by [1]:

$$\ln(p/\mathrm{Pa}) = A + BT^{-1} + C\ln(T) + DT^{-3} \tag{2.4}$$

The coefficients A-D are experimentally determined constants. Given the vapor pressure

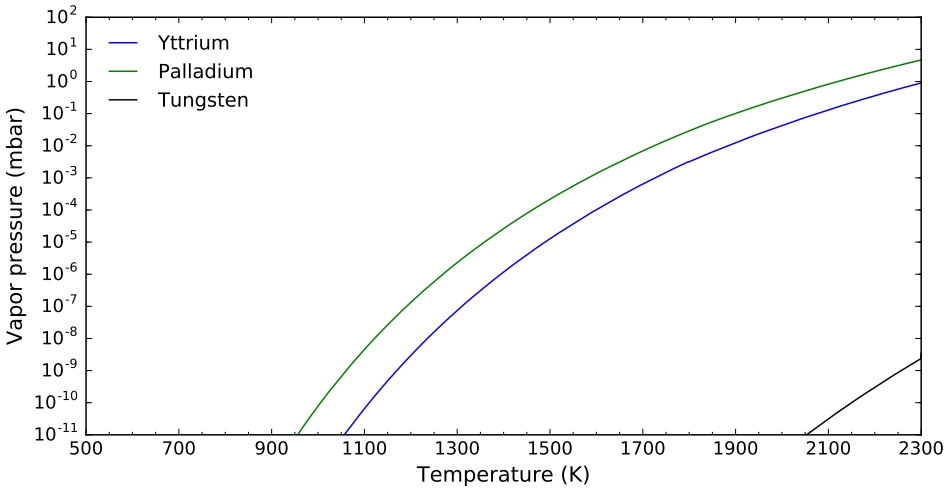

Figure 2.1: Vapor pressure curves for yttrium, palladium and tungsten. Data from [1].

of a material at a certain temperature, its rate of evaporation can be calculated with the Hertz-Knudsen equation [14]:

$$\varphi = \frac{(p_\mathrm{v} - p_\mathrm{a})}{\sqrt{2\pi MRT}} \tag{2.5}$$

where φ is the molar flux of the gas molecules, $p_\mathrm{v} - p_\mathrm{a}$ the difference between the vapor pressure p_v and the ambient pressure p_a, and M the molar mass of the evaporant. The total rate of evaporation is calculated by integrating over the evaporant surface area A_e:

$$\frac{\mathrm{d}m_\mathrm{e}}{\mathrm{d}t} = M \int_{A_\mathrm{e}} \varphi \, \mathrm{d}A_\mathrm{e} \tag{2.6}$$

The mass deposition rate per area onto a substrate of area $\mathrm{d}A_\mathrm{s}$ at a distance r from the evaporation source (see fig. 2.2) can be calculated by:

$$\frac{\mathrm{d}m_\mathrm{s}}{\mathrm{d}t\mathrm{d}A_\mathrm{s}} = \frac{dm_\mathrm{e}}{dt} \frac{\mathrm{d}A_\mathrm{s} \cos\theta \cos\varphi}{\pi r^2} \tag{2.7}$$

Important in the deposition process of optical films is thickness uniformity, which mainly depends on substrate size and distance from the source [10]. With increasing evaporation angle φ the deposition rate decreases (eq. 2.7). The thickness d can be calculated using the material density ρ and eq. 2.7:

$$d = \frac{m_\mathrm{e} \cos\theta \cos\varphi}{\pi\rho r^2} = \frac{m_\mathrm{e}}{\pi\rho r^2} \frac{h}{r} \frac{h}{r} = \frac{m_\mathrm{e} h^2}{\pi\rho(h^2 + l^2)^2} \tag{2.8}$$

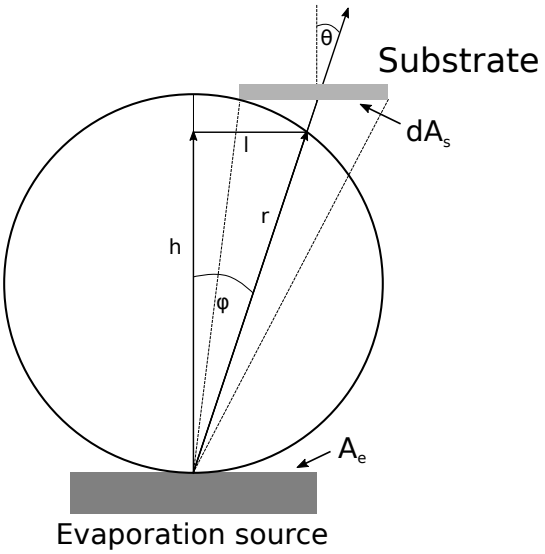

Figure 2.2: Evaporation from a surface source onto a substrate.

with $\cos\theta = \cos\varphi = \frac{h}{r}$ (see fig. 2.2). Relative to the thickest point, the density decreases with l, following:

$$\frac{d}{d_0} = \frac{1}{(1 + (l/h)^2)^2} \tag{2.9}$$

Considering the evaporator setup that will be used in this work ($l_{\max} = 5\,\text{mm}$, $h = 93\,\text{mm}$) the maximum variation in thickness due to evaporation geometry is $0.5\,\%$.

2.2 Characteristics of Thin Film Optical Spectra

2.2.1 Light-Matter Interaction

Electromagnetic waves propagating through a medium will accelerate any charged particles present, resulting in a polarization of the medium, which in turn generates additional electric fields. Understanding this interaction between light and matter is the goal of this chapter.
A starting point will be the four Maxwell equations for macroscopic electromagnetism [9]:

$$\nabla \cdot \vec{D} = \rho_{\text{ext}} \tag{2.10}$$

$$\nabla \cdot \vec{B} = 0 \tag{2.11}$$

$$\nabla \times \vec{E} = -\frac{\partial \vec{B}}{\partial t} \tag{2.12}$$

$$\nabla \times \vec{H} = \vec{J}_{\text{ext}} + \frac{\partial \vec{D}}{\partial t} \tag{2.13}$$

which make a connection between the macroscopic fields $\vec{D}$ (dielectric displacement), $\vec{E}$ (electric field), $\vec{H}$ (magnetic field) and $\vec{B}$ (magnetic flux density or magnetic induction), and external charge $\rho_{\text{ext}} = \rho_{\text{tot}} - \rho$ and external current density $\vec{J}_{\text{ext}} = \vec{J}_{\text{tot}} - \vec{J}$ (with (ρ,$\vec{J}$) describing the internal response of a material to external stimuli).
Polarization $\vec{P}$ and magnetization $\vec{M}$ further link the macroscopic fields together:

$$\vec{D} = \varepsilon_0 \vec{E} + \vec{P} \tag{2.14}$$

$$\vec{H} = \frac{1}{\mu_0}\vec{E} + \vec{M} \tag{2.15}$$

where ε_0 is the vacuum permittivity and μ_0 the magnetic permeability of vacuum. Exposed to an external electric field, any dipoles present in a material will try to align along the field direction. This can be expressed by [16]:

$$\vec{P} = \varepsilon_0 \chi_{\text{e}} \vec{E} \tag{2.16}$$

where χ_e is the dielectric susceptibility of a material. The same case can be made for the magnetization $\vec{M}$:

$$\vec{M} = \chi_{\text{m}} \vec{H} \tag{2.17}$$

with χ_m being the magnetic susceptiblity. Eq. 2.16 and eq. 2.17 both require a linear relationship between the external field and the internal response, they do not hold true for all cases.
Combining eq. 2.14 with eq. 2.16, and eq. 2.15 with eq. 2.17 respectively, one can define:

$$\vec{D} = \varepsilon_0 \varepsilon \vec{E} \tag{2.18}$$

$$\vec{B} = \mu_0 \mu \vec{H} \tag{2.19}$$

with $\varepsilon = 1 + \chi_e$ being the relative permittivity or dielectric function and $\mu = 1 + \chi_m$ the magnetic permeability.
Materials in this work will be largely non-magnetic, thus $\mu = 1$ will be assumed for the following derivations.
Equipped with these equations one can have a look at traveling-wave solutions of Maxwell's equations. Assuming no external stimuli $J_{ext} = 0$ and $\rho_{ext} = 0$, combining the curl equation 2.12 and 2.13 leads to:

$$\nabla \times \nabla \times \vec{E} = -\mu_0 \frac{\partial^2 \vec{D}}{\partial t^2} \tag{2.20}$$

in the time domain, and:

$$\vec{k}(\vec{k}\cdot\vec{E}) - \vec{k}^2\vec{E} = -\varepsilon(\vec{k},\omega)\frac{\omega^2}{c^2}\vec{E} \tag{2.21}$$

in the frequency, domain using $\frac{\partial}{\partial t} \rightarrow -i\omega$. With $c = \frac{1}{\sqrt{\varepsilon_0\mu_0}}$ being the speed of light.
From this, the dispersion relation for transverse waves ($\vec{k}\cdot\vec{E} = 0$) can be obtained:

$$\vec{k}^2 = \varepsilon(\vec{k},\omega)\frac{\omega^2}{c^2} \tag{2.22}$$

while for longitudinal waves, eq. 2.21 leads to:

$$\varepsilon(\vec{k},\omega) = 0 \tag{2.23}$$

The interaction of a material with electromagnetic waves can be fully described by the dielectric function of that material, which, in general, is frequency dependent and has a real and an imaginary part:

$$\varepsilon = \varepsilon(\omega) = \varepsilon_1(\omega) + i\varepsilon_2(\omega) \tag{2.24}$$

Important for experimental determination is the relationship between the dielectric function and the refractive index $\hat{n}(\omega) = n(\omega) + i\kappa(\omega)$ defined as $\hat{n} = \sqrt{\varepsilon}$ (assuming $\mu = 1$). Using this relationship leads to:

$$\varepsilon_1 = n^2 - \kappa^2 \tag{2.25}$$

$$\varepsilon_2 = 2n\kappa \tag{2.26}$$

$$n^2 = \frac{\varepsilon_1}{2} + \frac{1}{2}\sqrt{\varepsilon_1^2 + \varepsilon_2^2} \tag{2.27}$$

$$\kappa = \frac{\varepsilon_2}{2n} \tag{2.28}$$

If a homogeneous media is assumed, in the sense that the dielectric function does not depend on position, a general solution to the wave equation 2.21 has the form:

$$\vec{E} = \vec{E}_0 e^{-i(\omega t - \vec{k}\vec{r})} \tag{2.29}$$

Non-trivial solutions exist for:

$$k = \pm\frac{\omega}{c}\sqrt{\varepsilon} \tag{2.30}$$

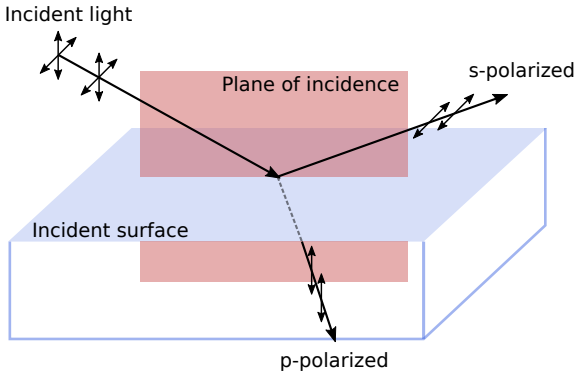

Figure 2.3: s and p-polarizations are defined by their orientation relative to the plane of incidence. Inspired from [8].

For a planar wave travelling along the x-axis this leads to (using $\sqrt{\varepsilon} = n(\omega) + i\kappa(\omega)$):

$$\vec{E} = \vec{E}_0 e^{-i(\omega t - \frac{\omega}{c}\sqrt{\varepsilon}x)} = \vec{E}_0 e^{-\frac{\omega}{c}\kappa} e^{-i(\omega t - \frac{\omega}{c}nx)} \tag{2.31}$$

with $\vec{E}_0$ representing the amplitude for $x = 0$. Equation 2.31 makes it clear why κ is called the extinction coefficient, as it describes the damping of an electromagnetic wave propagating through the material while n quantifies the change in phase velocity.

2.2.2 Optical Properties of Thin Films

Deriving the optical properties of a thin film system starts with the Fresnel equations, which describe the reflection and transmission of electromagnetic radiation incident on an interface. These can be derived using Maxwell's equations 2.10 to 2.13 combined with the condition, that the tangential component of $\vec{E}$ and $\vec{H}$ both have to be continuous, a complete derivation can be found in [16].
The first step is to split the electric field $\vec{E}$ and the magnetic field $\vec{H}$ up into components parallel ($\vec{E}_\mathrm{p}$,$\vec{H}_\mathrm{p}$), (p-component); and normal ($\vec{E}_\mathrm{s}$,$\vec{H}_\mathrm{s}$), (s-component) to the plane of incidence, which is defined as the plane which contains both the surface normal vector of the interface and the propagation vector of the incident electromagnetic wave. The geometry is shown in fig. 2.3. Superscripts denote incident (E), reflected (R) and transmitted (T) light.
The Fresnel equations are:

$$r_\mathrm{p} = \frac{E_\mathrm{p}^{(\mathrm{R})}}{E_\mathrm{p}^{(\mathrm{E})}} = \frac{\hat{n}_2 \cos\varphi - \hat{n}_1 \cos\psi}{\hat{n}_2 \cos\varphi + \hat{n}_1 \cos\psi} \tag{2.32}$$

$$r_\mathrm{s} = \frac{E_\mathrm{s}^{(\mathrm{R})}}{E_\mathrm{s}^{(\mathrm{E})}} = \frac{\hat{n}_1 \cos\varphi - \hat{n}_2 \cos\psi}{\hat{n}_1 \cos\varphi + \hat{n}_2 \cos\psi} \tag{2.33}$$

$$t_\mathrm{p} = \frac{E_\mathrm{p}^{(\mathrm{T})}}{E_\mathrm{p}^{(\mathrm{E})}} = \frac{2\hat{n}_1 \cos\varphi}{\hat{n}_2 \cos\varphi + \hat{n}_1 \cos\psi} \tag{2.34}$$

$$r_\mathrm{s} = \frac{E_\mathrm{s}^{(\mathrm{T})}}{E_\mathrm{s}^{(\mathrm{E})}} = \frac{\hat{n}_1 \cos\varphi}{\hat{n}_1 \cos\varphi + \hat{n}_2 \cos\psi} \tag{2.35}$$

Using these equations one can easily calculate the expected transmittance and reflectance of an electromagnetic wave incident on an interface between two media with different (possibly complex) refractive indices. With the intensity I of an electromagnetic wave given as:

$$I = \frac{\mathrm{Re}(\hat{n})\varepsilon_0 c_0}{2} |\vec{E}_0|^2 \tag{2.36}$$

The reflectance R for the geometry shown in fig. 2.4a is given by:

$$R_\mathrm{p} = \frac{I_\mathrm{p}^{(\mathrm{R})}}{I_\mathrm{p}^{(\mathrm{E})}} = \frac{|E_\mathrm{p}^{(\mathrm{R})}|^2}{|E_\mathrm{p}^{(\mathrm{E})}|^2} = \frac{|E_\mathrm{p}^{(\mathrm{E})} r_\mathrm{p}|^2}{|E_\mathrm{p}^{(\mathrm{E})}|^2} = |r_\mathrm{p}|^2 = \left| \frac{\hat{n}_2 \cos\varphi - \hat{n}_1 \cos\psi}{\hat{n}_2 \cos\varphi + \hat{n}_1 \cos\psi} \right| \tag{2.37}$$

$$R_\mathrm{s} = |r_\mathrm{s}|^2 = \left| \frac{\hat{n}_1 \cos\varphi - \hat{n}_2 \cos\psi}{\hat{n}_1 \cos\varphi + \hat{n}_2 \cos\psi} \right|^2 \tag{2.38}$$

For the transmittance the change in beam width that coincides with the change in propagation angle, altering the beam width, has to be taken into account (see fig. 2.4b).

$$\begin{aligned} T_\mathrm{s/p} &= \frac{\text{transmitted Intensity}}{\text{incident Intensity}} = \frac{I_\mathrm{T} w_\mathrm{T}}{I_\mathrm{E} w_\mathrm{E}} \\ &= \mathrm{Re}\left(\frac{\hat{n}_2 \cos\psi}{\hat{n}_1 \cos\varphi} \right) |t_\mathrm{s/p}|^2 \end{aligned} \tag{2.39}$$

Expanding the model from a single interface to that of an electromagnetic wave incident on a slab of thickness d (fig. 2.5) two interfaces have to be considered along with the phenomena of absorption and interference. Inside the slab the electromagnetic wave is given by:

$$\vec{E} = \vec{E}_0 e^{-i(\omega t - k_x x - k_z z)} = \vec{E}_0 e^{-i(\omega t - \frac{\omega}{c}\hat{n}_2 \sin\psi x - \frac{\omega}{c}\hat{n}_2 \cos\psi z)} \tag{2.40}$$

With Snell's law $\hat{n}_1 \sin\varphi = \hat{n}_2 \sin\psi$ eq. 2.40 can be rewritten as:

$$\vec{E} = \vec{E}_0 e^{-i(\omega t - \frac{\omega}{c}\hat{n}_1 \sin\varphi x - \frac{\omega}{c}\hat{n}_2 \cos\psi z)} = \vec{E}_0 e^{i\delta} \tag{2.41}$$

with δ representing the accumulated phase when propagating from one interface to the other. This modifies the Fresnel coefficients, as electromagnetic waves incident on the

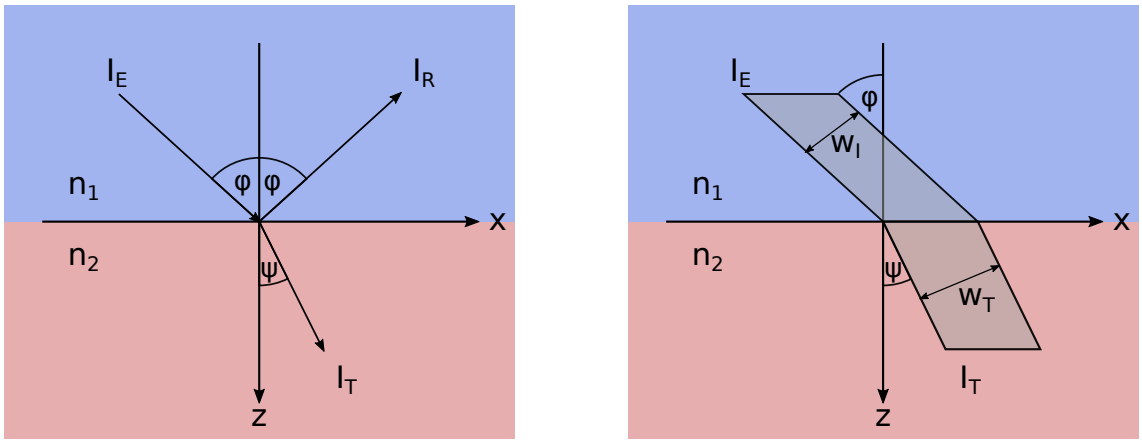

(a) Assumed geometry for the calculation of the reflectance.

(b) The beam width changes on refraction at the interface. The ratio of beam widths is given by $w_\mathrm{I} \cos\varphi = w_\mathrm{T} \cos\psi$.

Figure 2.4: Assumed geometry of light interacting with an interface between two media.

second interface will have to have propagated through the medium to get there.

$$t_{21} \to t_{21} e^{i\delta} \tag{2.42}$$

$$r_{21} \to r_{21} e^{i\delta} \tag{2.43}$$

With these modifications it is possible to calculate the total transmission and reflectance for the geometry in fig. 2.5. As the light may bounce several times from interface to interface inside the slab, all possible light paths need to be taken into account. The total Fresnel coefficients are then given by:

$$\begin{aligned} r_{123} &= r_{12} + t_{12} e^{i\delta} r_{23} e^{i\delta} t_{21} + t_{12} e^{i\delta} r_{23} e^{i\delta} r_{21} e^{i\delta} r_{23} e^{i\delta} t_{21} + \ldots \\ &= r_{12} + t_{12} r_{23} t_{21} e^{2i\delta} \sum_{j=0}^{\infty} (r_{21} r_{23} e^{2i\delta})^j \\ &= r_{12} + \frac{t_{12} r_{23} t_{21} e^{2i\delta}}{1 - r_{21} r_{23} e^{2i\delta}} \end{aligned} \tag{2.44}$$

$$\begin{aligned} t_{123} &= t_{12} t_{23} e^{i\delta} + t_{12} r_{23} e^{i\delta} r_{21} e^{i\delta} t_{23} e^{i\delta} + \ldots \\ &= t_{12} t_{23} e^{i\delta} \sum_{j=0}^{\infty} (r_{23} r_{21} e^{i2\delta})^j \\ &= \frac{t_{12} t_{23} e^{i\delta}}{1 - r_{23} r_{21} e^{i2\delta}} \end{aligned} \tag{2.45}$$

Important to consider when dealing with any interference phenomenon is the coherence length. For a light beam travelling from the first interface to the second one and back

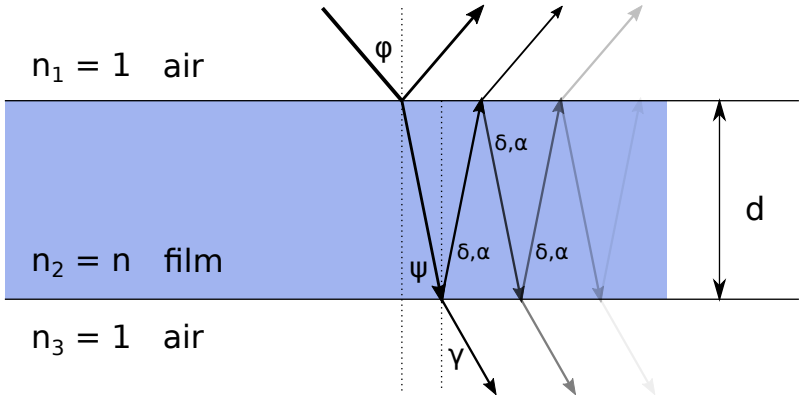

Figure 2.5: Incident on the first interface, the light can be either transmitted or reflected. In the case of transmission, the beam can again be transmitted or reflected at the second interface, ultimately resulting in infinitely many possible light paths, that all have to be taken into account when calculating the total transmittance or reflectance.

the travelling time assuming normal incidence will be $t = 2nd/c$. If the travelling time t is larger than the coherence time t_{coh} of the light, no interference will be observed. This requires:

$$t = \frac{2nd}{c} > t_{\text{coh}} \tag{2.46}$$

With the relation:

$$\Delta\omega = \frac{2}{t_{\text{coh}}} = \frac{2\pi c}{\lambda^2}\Delta\lambda \tag{2.47}$$

the condition for the observation of any interference phenomenon can by expressed by:

$$d > \frac{\lambda^2}{2\pi n \Delta\lambda} \tag{2.48}$$

which defines the thick slab condition. In the case that eq. 2.48 holds only the damping part of the accumulated phase has to be considered while interference can be neglected. The change in intensity for a light beam travelling from one interface to the other can be calculated using eq. 2.41:

$$\begin{aligned} I(z=d) \propto |\vec{E}|^2 &= |\vec{E}_0|^2(z=d)e^{-2\frac{\omega}{c}(\hat{n}_2\cos\psi)d} \\ &= |\vec{E}_0|^2 e^{-2\frac{\omega}{c}d\,\mathrm{Im}\sqrt{\hat{n}_2^2-\hat{n}_1^2\sin^2\varphi}} \\ &= |\vec{E}_0|^2 e^{-2\alpha d} \end{aligned} \tag{2.49}$$

This damping has to be incorporated into the Fresnel coefficients for a thick slab, modifying eq. 2.43 to:

$$t_{21} \rightarrow t_{21}e^{-\alpha d} \tag{2.50}$$

$$r_{21} \rightarrow r_{21}e^{-\alpha d} \tag{2.51}$$

Now onto the final case of a thin film on a thick substrate with air on either side, as will be the case for transmission measurements. The geometry is shown in fig. 2.6. Again every

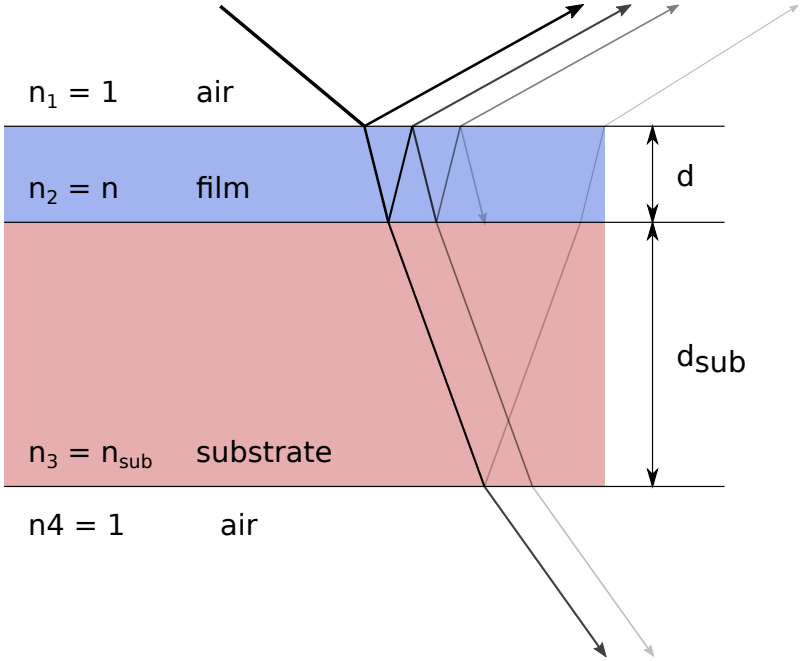

Figure 2.6: Schematic of a thin film on a thick substrate.

possible light path has to be considered. The Fresnel coefficients from eq. 2.45 already deal with all light paths inside the thin film. Accounting for the possible light path inside the thick substrate leads to the following expression for the total Fresnel coefficients for the multilayer system:

$$\begin{aligned} t &= t_{123}t_{31}e^{-\alpha d} + t_{123}r_{31}e^{-\alpha d}r_{321}e^{-\alpha d}t_{31} + t_{123}(r_{31}e^{-\alpha d}r_{321}e^{-\alpha d})^2 t_{31} + ... \\ &= t_{123}t_{31}e^{-\alpha d}\sum_{j=0}^{\infty}(r_{31}r_{321}e^{-2\alpha d})^j = \frac{t_{123}t_{31}e^{-\alpha d}}{1 - r_{31}r_{321}e^{-2\alpha d}} \end{aligned} \tag{2.52}$$

$$\begin{aligned} r &= r_{123} + t_{123} r_{31} e^{-\alpha d} r_{321} e^{-\alpha d} t_{321} + t_{123} (r_{31} e^{-\alpha d} r_{321} e^{-\alpha d})^2 t_{321} + ... \\ &= r_{123} + t_{123} r_{31} r_{321} t_{321} e^{-2\alpha d} \sum_{j=0}^{\infty} (r_{321} r_{31} e^{-2\alpha d})^j \\ &= r_{123} + \frac{t_{123} r_{31} t_{321} e^{-2\alpha d}}{1 - r_{321} r_{31} e^{-2\alpha d}} \end{aligned} \tag{2.53}$$

Combining these with the equations 2.39 and 2.38 the transmittance and reflectance for such a system (fig. 2.6) can be calculated if the refractive indices, as well as the incidence angle are known.

2.3 Hydrogen Induced Phase Change of Yttrium

As the main goal of this work is to observe the Metal-to-Insulator (MI) phase transition of yttrium when exposed to hydrogen, this section will go over the different YH_x phases and their properties.

Figure 2.7a shows a schematic of the Y-H phase diagram while fig. 2.7b depicts changes in resistivity during hydrogen loading as well as changes in optical transmission for a single wavelength (689 nm). Simple yttrium in the α-phase ($x = 0$) is a metal in hcp-structure, shown in fig. 2.8a, where for low x, hydrogen atoms are distributed on the tetrahedral interstitial sites (T-sites). These hydrogen atoms act as scattering centers, increasing resistivity along with the hydrogen ratio up to the phase limit (see 2.7a).

For $x > 0.24$ at room temperature, the β-phase starts to precipitate, which crystallizes in the fcc structure Fm3m, shown in fig. 2.8c, with hydrogen in the T-sites [13]. This phase change is accompanied by a drop in resistivity (fig. 2.7b), as the dihydride phase has a resistivity about 5 times lower than pure yttrium [7], the main reason being reduced electron phonon coupling [13]. Beyond $x = 2$, the octahedral sites in the fcc lattice start to fill with hydrogen and the γ-phase starts to form (in hcp structure, see fig. 2.8e) coexisting with the β-phase up to $x = 2.75$ [12]. The exact space group of the γ-phase beyond $x = 2.75$ is still unclear, however Udovic et al. [20] determined the space group of YD_3 (exchanging hydrogen with deuterium) to be $P\bar{3}c1$ which is shown in fig. 2.8e. The phase change towards the γ-phase is accompanied by an increase in resistivity as well as an increase in transmission (fig. 2.7b), suggesting that the YH_3 is semiconducting. This has been confirmed by Huiberts et. al, who measured the band gap to be about 1.8 eV. The metallic character of the α- and β-phase can also be observed in the dielectric functions (see fig. 2.8b and 2.8d), as they both have negative real parts. For YH_3 the metallic properties vanish (see fig. 2.8f), providing further evidence for the semiconducting nature of the γ-phase.

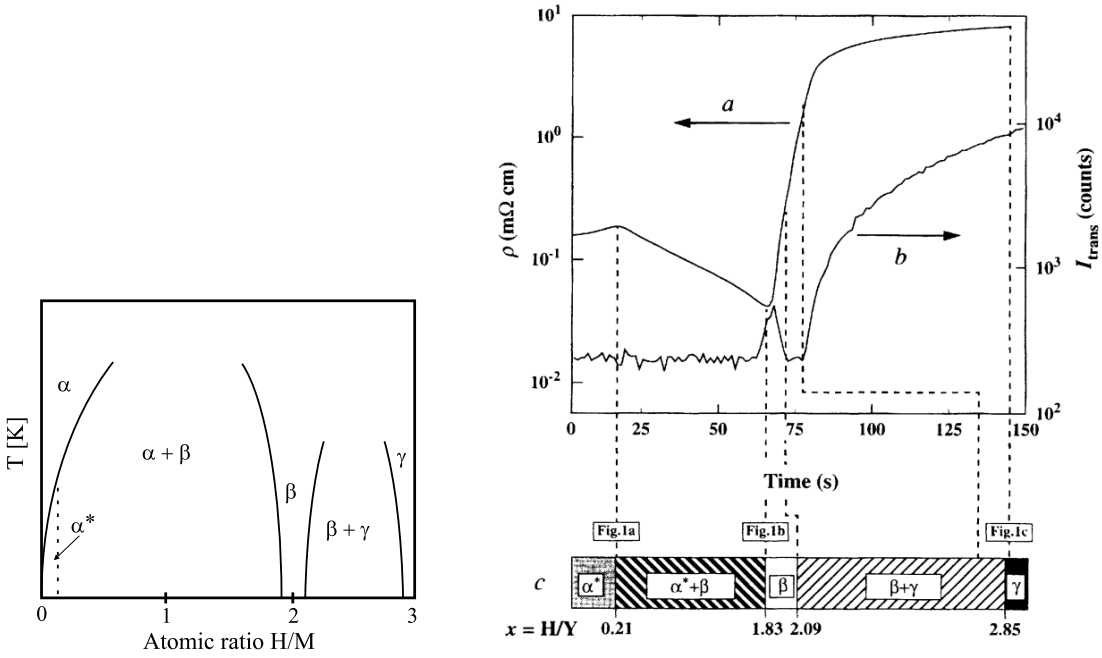

(a) Schematic of the Y-H phase diagram [21].

(b) Resistivity and transmitted Intensity change during hydrogen loading [7].

Figure 2.7: **(a)** shows how the yttrium phase is dependent on temperature and atomic ratio. **(b)** shows measurements of the resistivity and transmitted intensity of an yttrium film during hydrogen loading.

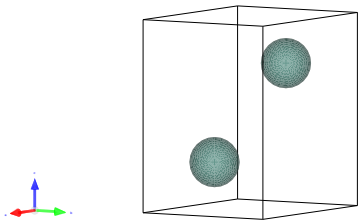

(a) Y α-phase in space group P6$_3$mmc [6].

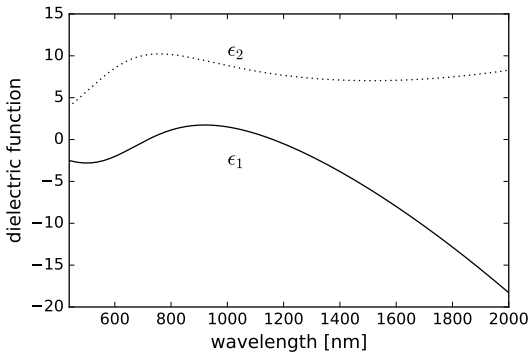

(b) dielectric function for Y [3].

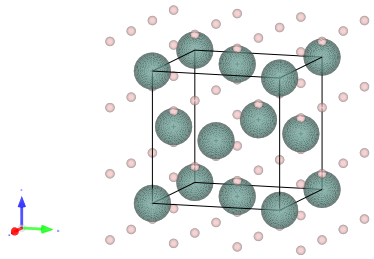

(c) β-phase in space group Fm3m [6].

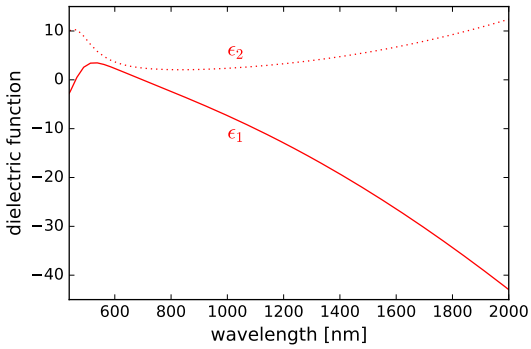

(d) dielectric function for YH_2 [18].

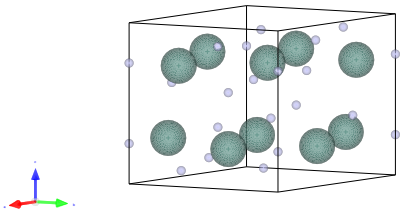

(e) YD_3 in space group P$\bar{3}$c1 [6].

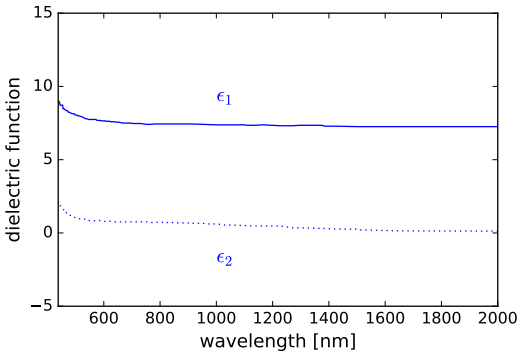

(f) dielectric function for YH_3 [5].

Figure 2.8: Crystal structures and dielectric function for the different phases of YH_x.

3 Materials and Methods

This chapter will go over the different experimental methods used in this work.
Thin films were produced using electron-beam physical vapor deposition.
Optical characterisations include measurements of transmission spectra during hydrogen exposure, as well as fourier-transform infrared spectroscopy (FTIR).
Atomic force microscopy (AFM) was used to measure film thickness.

3.1 Evaporation

3.1.1 Ultra-High Vacuum Chamber

All evaporations took place in a custom built, ultra-high vacuum (UHV) chamber, capable of pressures as low as 10^{-10} mbar using a turbomolecular pump.

3.1.2 Evaporation materials

As yttrium oxidizes when exposed to air, a cover layer out of palladium is needed, which doubles as a catalyst for splitting up hydrogen molecules at its surface. Source materials will be placed inside a crucible that is heated to high temperatures during the deposition process. The right crucible for a given material can be found in [2]. Though the crucible-evaporant interaction still has to be carefully monitored and experimenting with different crucible materials may be required. Tungsten crucibles are used for the evaporation of yttrium and palladium, as tungsten has a low vapor pressure (see fig. 2.1) ensuring that it is not co-evaporated along with yttrium or palladium.

3.1.3 Thermal Evaporator - EFM 3T

For evaporation, a thermal evaporator (EFM 3T from FOCUS GmbH) is used, which features three independent cells (fig. 3.3) allowing for the evaporation of up to three different materials without ventilating the chamber to exchange materials, which would expose any yttrium layer to oxygen and destroy its functionality. The EFM 3T operates by bombarding a target anode (tungsten crucible) with an electron beam that is given off by a thin tungsten filament and accelerated by an applied high voltage. A schematic of such an operation cell is shown in fig. 3.3.

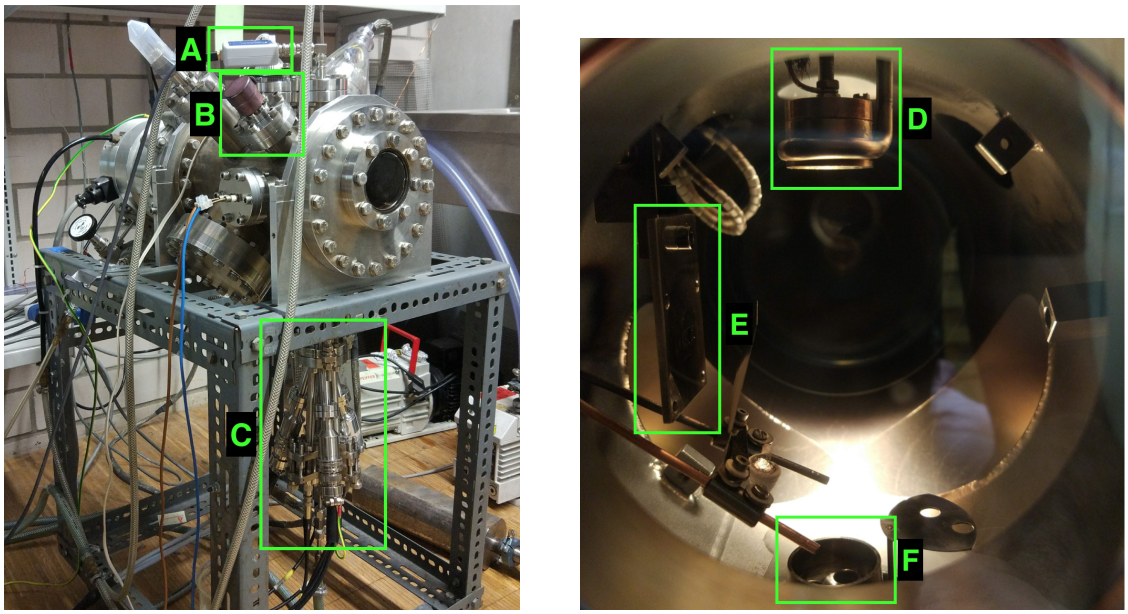

(a) **(b)**

Figure 3.1: Outer view **(a)** showing the UHV chamber and evaporation setup. A: readout electronics for quartz microbalance; B: sample control arm; C: EFM 3T Evaporator.
(b) is the inner view with D: quartz crystal microbalance; E: sample holder (in the inactive position); F: evaporator.

A power supply supplies both the filament current I_F, causing thermal emission of electrons, and the anode potential U. Electron energy upon impact is controlled by the anode potential, the impact rate by the emission current I_E. The temperature that the crucible (anode) will reach, depends on both size (more surface area allows for more energy to be radiated) and applied heating power P, given by:

$$P = I_F \cdot U \tag{3.1}$$

Estimations of crucible temperature depending on size and heating power are shown in fig. 3.4.
To measure the flow of particles that are evaporated, each cell is equipped with a flux monitor. Metal tubes pick up vapor particles that are ionized, registering them as an electric current I_F.
A necessary step prior to deposition is the degasification of the crucibles and source materials. In order to remove any impurities present that would evaporate and contaminate the film, a high heating power is applied for longer periods of time until most of the impurities have evaporated. The flux is a good indicator of evaporant purity, a decaying flux is a sign of impurities evaporating (see fig. 4.1).

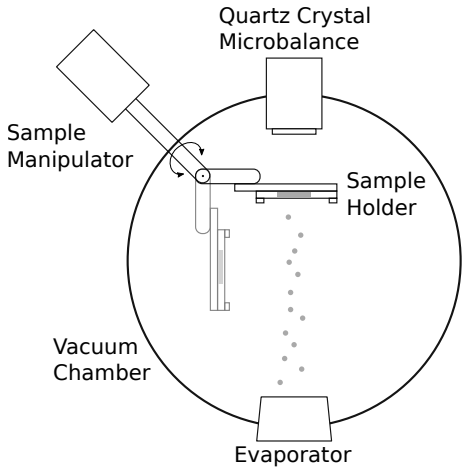

Figure 3.2: Evaporation geometry from 3.1b. For measurements with the quartz crystal the sample holder has to be turned into the inactive position.

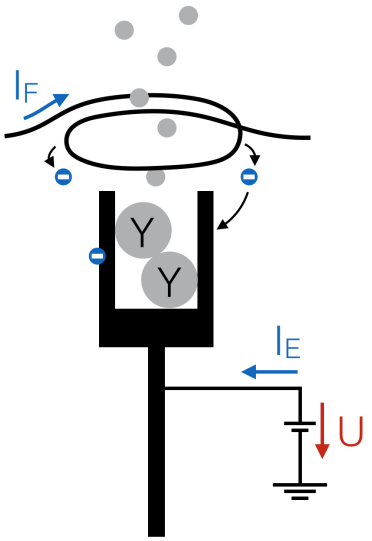

Figure 3.3: The filament current I_F causes thermal emission from the filament, producing free electrons that are accelerated due to the high voltage U applied to the crucible and transfer energy upon impact. At sufficiently high temperatures the yttrium inside starts to evaporate.

3.1.4 Quartz Crystal Microbalance

To measure the effective rates of deposition onto the substrates, a quartz crystal microbalance uses the piezoelectric effect to measure changes in resonance frequency of a quartz crystal. The resonance frequency f depends on the mass m of the crystal, thus changes over time as material is deposited. The Sauerbrey equation correlates small changes in

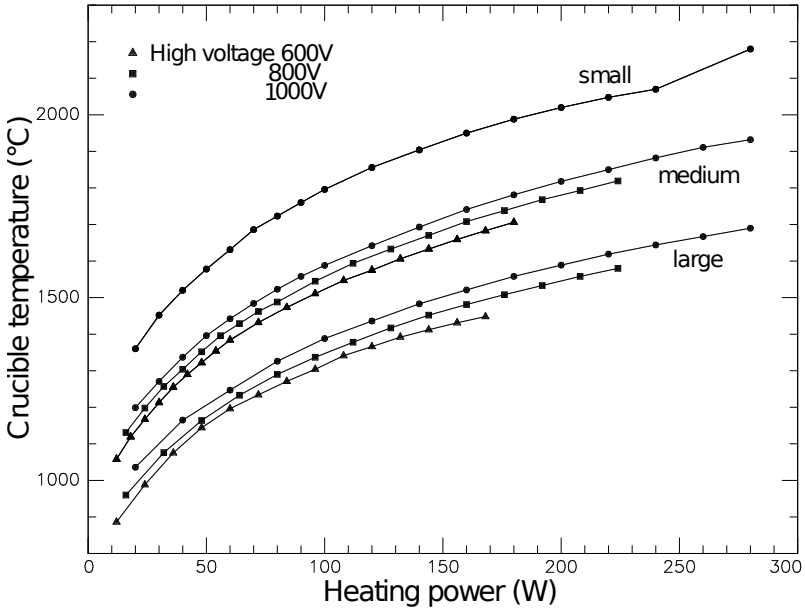

Figure 3.4: Diagram showing the crucible temperature as a function of heating power for different crucible sizes. Crucibles used in this work correspond to the "medium" graph. Figure from [4].

mass Δm with changes in resonance frequency Δf: [19]

$$\Delta f = -\frac{2f_0^2}{A\sqrt{\rho_q \mu_q}}\Delta m \tag{3.2}$$

Assuming uniform coverage, the rate of deposition R can be calculated by:

$$R = \frac{\Delta m}{\rho_\mathrm{f} \Delta t} \tag{3.3}$$

where ρ_f denotes the evaporant density. During evaporation the deposition rate R multiplied by the total evaporation time t_evap is the sole indicator of film thickness. Thus a stable deposition rate is crucial to ensure the that the film thickness can be accurately estimated. Unfortunately, the setup does not allow for simultaneous deposition onto the sample and measurement of the deposition rate (see fig. 3.2). To maintain stable deposition rates during evaporation, thorough degasification of the source materials prior to evaporation is required, so that a stable equilibrium is reached and the evaporation of unwanted impurities is kept to a minimum.

3.2 Sample Preparation

SiO_2 covered by a thin (20 nm) indium tin oxide (ITO) layer is used as a substrate. Substrates are cleaned using acetone prior being placed into the sample holder that is then mounted inside the UHV chamber (see fig. 3.5). To leave a blank reference area, needed for the optical measurements, the sample holder features a metal bar to prevent a part of the substrate surface from being covered in the deposition process. After a stable

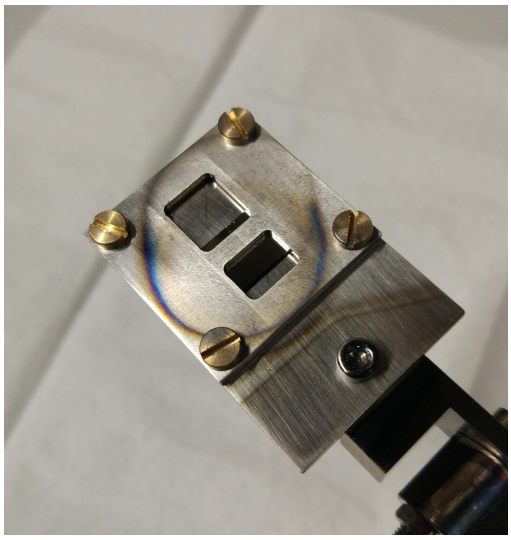

Figure 3.5: A custom sample holder that prevents part of the substrate from being covered during evaporation. This leaves a blank area on the substrate that will be used as a reference in transmission measurements.

deposition rate is monitored over several minutes the sample is rotated into the vapor beam (fig. 2.2). Film thickness is estimated using the deposition rate and duration of the deposition process. After depositing the yttrium layer in this manner, the palladium is deposited right after, using the same method to prevent the yttrium layer from oxidizing.

3.3 Spectroscopy

The hydrogen induced phase change of yttrium has a large effect on the optical properties and can therefore be observed by conducting transmission measurements throughout the hydrogen loading process.
For the optical measurements a transmission microscope from NT&C was used. Measurements conducted are relative transmission spectra with the bare substrate as reference to correct for the influence of the experimental setup on the spectrum. To make *in-situ* transmission measurements possible, the samples were mounted inside a gas cell (fig. 3.6) that is connected to an electronically controlled gas system, which allows precise control

over gas flow and composition. To drive the phase transition, the samples were exposed to a hydrogen-nitrogen mixture (between 5 vol% and 20 vol% H_2). Otherwise a pure nitrogen environment is used to prevent oxidation of the samples. Detailed information about the microscope, gas cell and gas system can be found in [15].

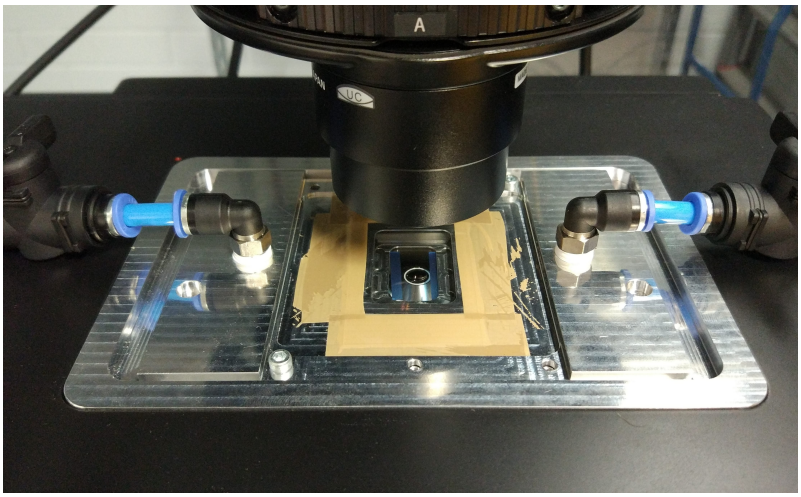

Figure 3.6: Gas cell used for *in-situ* measurements. The sample is mounted between two glass slides allowing for transmission measurements, while gas flow through the chamber is controlled via an external gas system.

3.4 Atomic Force Microscope

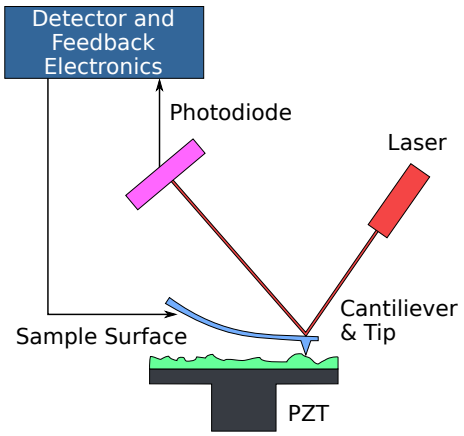

Figure 3.7: Schematic of an Atomic Force Microscope [11].

To investigate the physical dimensions of the produced samples, an atomic force microscope (AFM) is used. The basic principle of operation is shown in fig. 3.7. An AFM consists of a cantilever with a sharp tip, typically made of silicon, that has a radius of curvature of a few

nanometers. This tip, when close to the sample surface, experiences the sum of (depending on the situation) van der Waals forces, electrostatic forces, chemical bonding and others. Any movement of the tip changes the reflection angle of the laser that is focused onto the cantilever, which can be detected by a photodiode. In this way the thickness of the samples can be measured, using the substrate surface as a reference. To be able to measure film thickness with the AFM, using a sharp needle, part of the deposited film is removed from the substrate, creating the required reference area.

4 Experimental Results

The first measurements conducted were on evaporation behaviour for yttrium and palladium. Determining stable evaporation conditions is crucial to ensure a clean film deposition.
In the second part, measurements for each sample deposited will be shown. These include measurements of the transmittance shift induced by hydrogen exposure, as well as atomic force microscopy measurements to compare actual film thickness with estimations from the deposition process.

4.1 Evaporant Behaviour

Before deposition could begin, the evaporation behaviour had to be studied to ensure clean conditions. The process of degasification (removing impurities from the crucibles and source materials) is shown in the following subsections.

4.1.1 Crucibles

As a first step, the tungsten crucibles, which will subsequently act as a container for the source materials, were degassed, using a heating power of about 100W corresponding to a temperature of roughly 1500 °C, in order to remove as many impurities as possible. The flux I_F, as well as the emission current I_E measured over the course of the degasification procedure are shown in fig. 4.1. The flux, which measures particle flow, could be reduced down to several nA for high heating powers, suggesting that all impurities have evaporated and the crucible is clean. Higher temperatures during the degasification process are desired, as higher temperatures cause more impurities to evaporate, resulting in a cleaner end product. This shows one benefit of using tungsten as a crucible material, as very high temperatures can be achieved without the crucible itself evaporating.

4.1.2 Yttrium

The yttrium source material had to be broken up into smaller pieces in order to fit into the crucible, introducing impurities into the material in the process. As this also increased

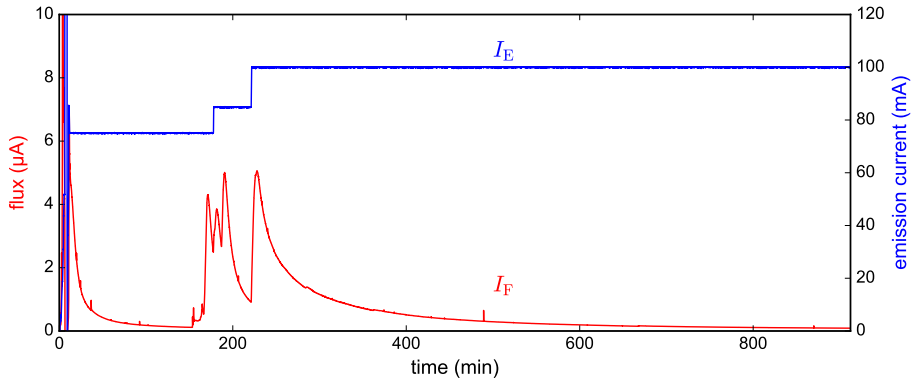

Figure 4.1: Degasification of one tungsten crucible, $U = 1000\,\mathrm{V}$. The emission current I_E controls the temperature. The flux I_F measures particle flow. Increasing the emission current leads to an increase in temperature, causing impurities to evaporate and be registered as an increase in the flux reading.

the surface area, a great portion of the yttrium source material had already oxidized prior to evaporation.

The result was a volatile degasification behaviour (fig. 4.2), where at the start, the emission current has to be carefully controlled to ensure that the evaporating impurities do not cause the UHV chamber pressure to raise above its critical limit ($\sim 10^{-6}\,\mathrm{mbar}$), where the heating filaments (3.3) used in the evaporator will start to break down. The time development of the flux has characteristics of an exponential decay, making it difficult to remove all impurities from the source material, as this would take a long time. Each time the emission current is increased, the increased temperature leads to the evaporation of a new set of impurities, causing a bump in the flux reading.

Achievable rates of deposition are up to $0.35\,\mathrm{Å/s}$ for a heating power of $P = 70\,\mathrm{W}$. Using a greater heating power would enable the usage of higher deposition rates, but also complicates the degasification, as more impurities co-evaporate at higher temperatures.

4.1.3 Palladium

Compared to yttrium, the palladium source material had much better characteristics, mainly due to palladium being chemically inert towards oxygen, preventing oxidation. Additionally the palladium comes in small pellets that fit right into the tungsten crucibles, reducing the surface area that could possibly carry contaminations. All this reflects in the degasification characteristics of Palladium, shown in fig. 4.3. The emission current could be increased much faster (compared to yttrium) while maintaining a low enough pressure for operation. Problems arise due to the evaporator setup, as the cell palladium was evaporated from, did tend to short circuit, causing sharp dips in the emission current (see

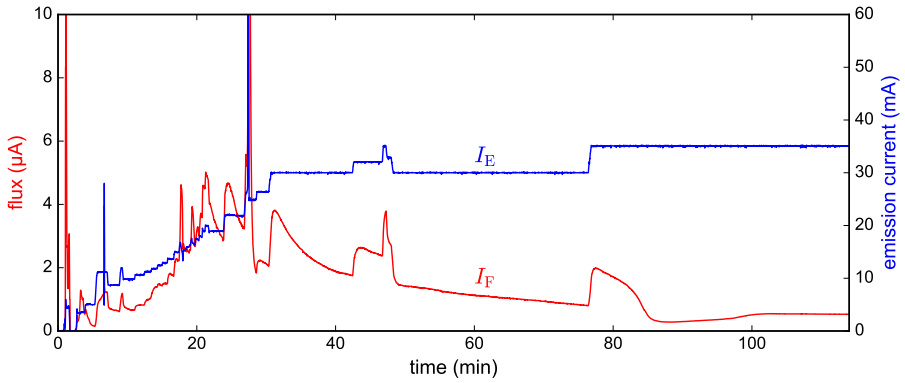

Figure 4.2: Degassing of Yttrium, $U = 1000\,\mathrm{V}$. Due to random short-circuiting the emission current sharply increases at $t = 30\,\mathrm{min}$ accompanied by an increase in flux due to the increased heating power. For $t = 100\,\mathrm{min}$ the evaporant is sufficiently degassed, as the flux no longer decays. Remaining flux is due to evaporating yttrium particles.

fig. 4.3 at 55 min). Typical evaporation rates for palladium are $0.07\,\mathrm{Å/s}$ for $P = 50\,\mathrm{W}$ though higher rates can be easily reached, as the source material is very clean.

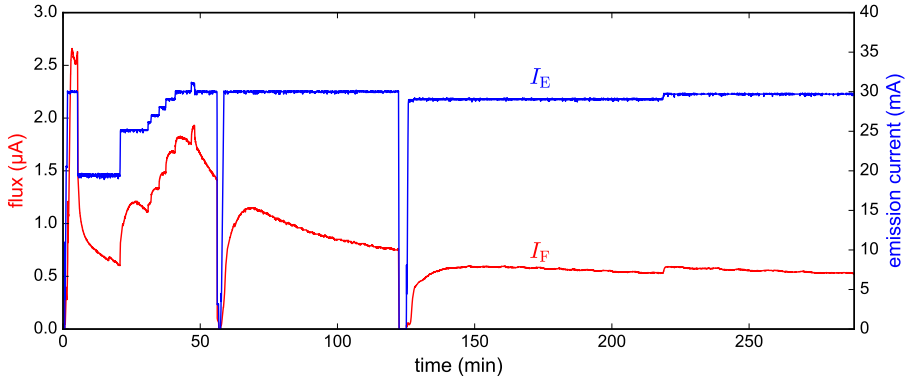

Figure 4.3: Degasification for palladium, $U = 1000\,\mathrm{V}$. Short circuits in the evaporator setup cause the power supply to cut off the emission current. For large t a plateau where the flux becomes constant due to the constant evaporation of palladium particles.

4.2 Film Behaviour

This section covers all measurements used to characterize the fabricated samples. Sample functionality was characterized using transmission spectroscopy, while morphology was investigated using atomic force microscopy. An overview of the samples is shown in tab. 4.1.

film no.	label	geometry Y/Pd in nm	purpose
1	F01	50/6	establish proof of concept
2	F02	50/6	1st optimization
3	F03	50/3	vary thickness of cover layer
4	Pd01	0/6	investigate cover layer properties
5	F04	50/6	2nd optimization
6	F05	50/6	check reproducibility

Table 4.1: Overview of all samples.

4.2.1 F01 - Proof of Concept

The first sample produced served to show, that a thin yttrium film covered with a protective layer of palladium would respond to hydrogen exposure. Tab. 4.2 shows evaporation parameters for F01. Only *ex-situ* measurements were possible at the time, conducted by exposing the sample to hydrogen in a gas cell and subsequent optical measurements. Starting out in Y phase right after deposition, an increase in transmittance is expected once the sample is exposed to hydrogen, as the transition Y $\longrightarrow$ YH_2 $\longrightarrow$ YH_3 takes place. Subsequently, the transmittance in expected to decrease over time, as the reversible transition, YH_3 $\longrightarrow$ YH_2, begins. No transition back into the Y phase is expected, as the Y $\longrightarrow$ YH_2 is irreversible. Fig. 4.4 shows the time development of the transmittance

	yttrium	palladium
rate (Å/s)	0.15 - 0.20	0.07 - 0.10
pressure range (10^{-8} mbar)	2.3 - 24	3.4 - 4.6
duration (min)	52	11.5
expected thickness (nm)	50.1	6.0

Table 4.2: Evaporation parameters for F01.

for F01 over 45 minutes after 15 minutes of 5 vol% hydrogen exposure to induce the Y $\longrightarrow$ YH_3 transition. Comparing the spectra before (Y, black) and after hydrogenation (YH_3, blue) in fig. 4.4, a clear increase in transmittance can be observed, showing that a phase transition could be induced. Additionally the irreversibility of the Y $\longrightarrow$ YH_2 transition could be confirmed, as the transmittance does not revert to its original shape after the initial hydrogenation.

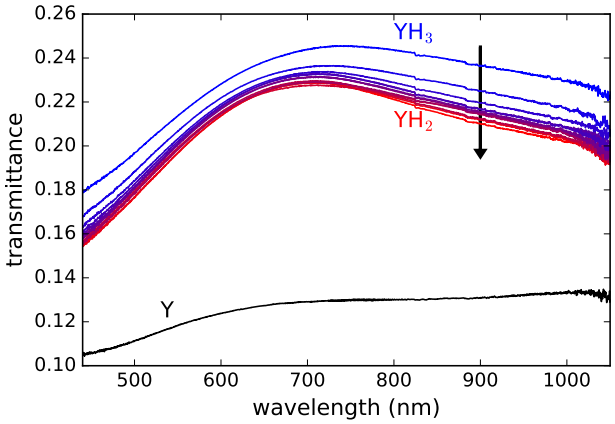

Figure 4.4: Transmittance measurements for each YH_x phase. After hydrogen exposure ends, the YH_3 phase starts to reverse back into the YH_2 phase (black arrow).

4.2.2 F02 - 1st Optimization

F02 was intended as a 50 nm thick yttrium film, covered by a 6 nm layer of palladium as protection to prevent oxidation. The main goal was to replicate results from [18].
Evaporation parameters are shown in table 4.3. Main differences between F02 and F01 regarding the deposition process, are more stable deposition rates and lower ambient pressures during deposition ($p_{\mathrm{F01,max}} = 2.4 \times 10^{-7}$ mbar vs. $p_{\mathrm{F02,max}} = 5.0 \times 10^{-8}$ mbar). A stable deposition rate should increase film homogenity, while lower ambient pressures reduce contaminations. Fig. 4.5 shows the transmittance shift for the reversible phase

	yttrium	palladium
rate (Å/s)	0.19 - 0.20	0.07
pressure range (10^{-8} mbar)	3.0 - 5.0	1.7 - 1.8
duration (min)	42.5	14.2
expected thickness (nm)	50.0	6.0

Table 4.3: Evaporation parameters for F02.

transitions $YH_2 \rightleftharpoons YH_3$. The $YH_2 \longrightarrow YH_3$ transition (in fig. 4.5a) takes 41 s when the sample is exposed to 5 vol% hydrogen. As the transition progresses, more of the dielectric phase YH_3 precipitates, increasing the transmittance of the sample. Fig. 4.5b shows the $YH_3 \longrightarrow YH_2$ transition, which starts right after hydrogen exposure ends. The transition from the dielectric YH_3 phase into the metallic YH_2 is much slower, taking place over 470 s of 100 vol% nitrogen exposure, and accompanied by a decrease in transmittance. Comparing both transmittance spectra, the reversibility of the two phases is again confirmed. Fig. 4.5 shows time traces for the transmittance at $\lambda = 700$ nm. In (a) the time

trace for the initial hydrogenation Y $\longrightarrow$ YH_2 $\longrightarrow$ YH_3 is shown, revealing that the Y to YH_2 transition happens much faster compared to the transition from YH_2 to YH_3. (b) shows the time trace for repeated cycles of hydrogen loading and unloading. With each cycle, the lower limit of the transmittance increases slighty (dashed line), suggesting that the hydrogen diffusion from the yttrium layer back through the palladium becomes more and more restricted. This may be a result of the yttrium layer slowly oxidizing in some areas, creating a barrier through which hydrogen can not diffuse as easily.

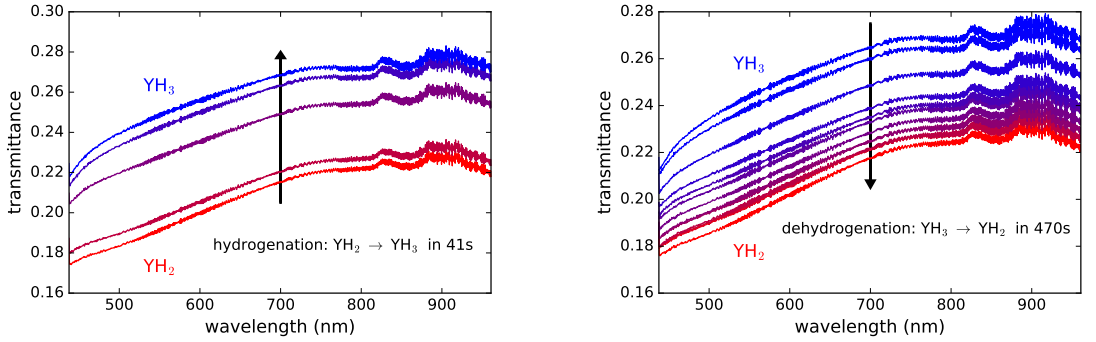

Figure 4.5: Transmittance shift over time for hydrogen loading **(a)** and unloading **(b)**.

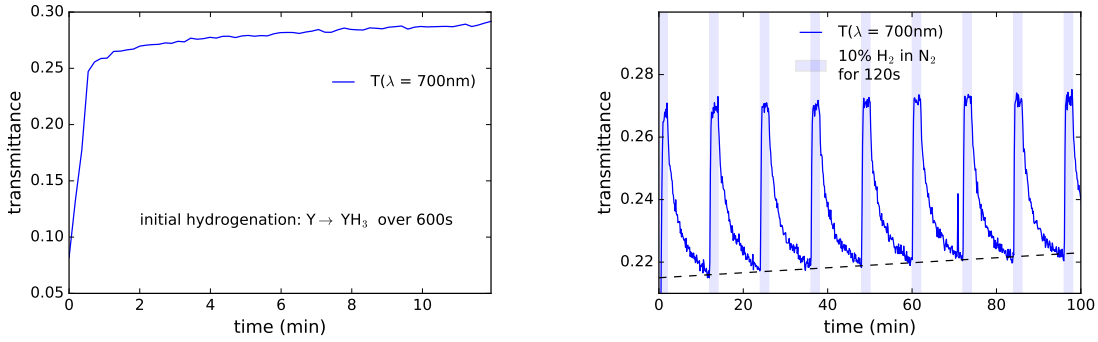

Figure 4.6: F02: Time traces of the transmittance for $\lambda = 700\,\text{nm}$. **(a)** shows the initial hydrogenation from the Y to YH_3 phase. Exposure to 5 vol% H_2 in N_2 for 600 s. **(b)** shows a time trace for repeated hydrogen loading and unloading.

AFM measurements (fig. 4.7a) reveal a film thickness of $(65.49 \pm 0.63)\,\text{nm}$, instead of the estimated 56 nm calculated from the measured deposition rate multiplied by evaporation time. To account for this, a so called tooling factor f is determined by:

$$f = \frac{\text{measured thickness}}{\text{expected thickness}} \tag{4.1}$$

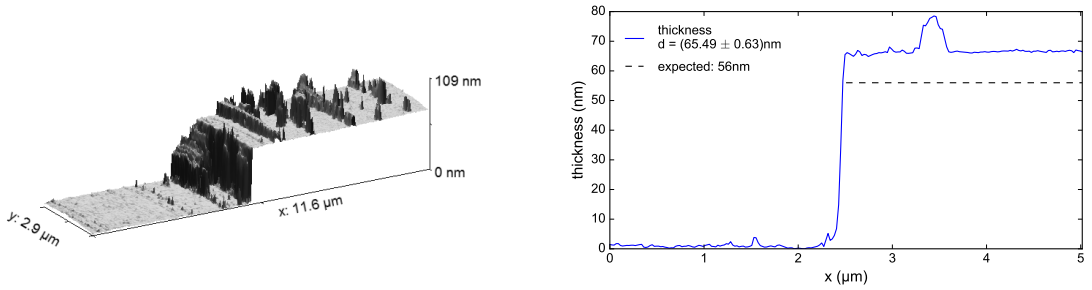

(a) **(b)**

Figure 4.7: AFM measurements on F02. **(a)** shows film topography with the intact film on the right, while it has been scratched away on the left. **(b)** is the thickness profile used to estimate film thickness. Dashed line represents the expected thickness.

which multiplied with the measured deposition rate will improve accuracy of the film thickness estimations. To calculate the tooling factors for palladium and yttrium, an additional AFM measurement for Pd01, a palladium film with an expected thickness of 6 nm was conducted (fig. 4.8a). Based on these two measurements, first estimations of the tooling factors for palladium and yttrium could be made: $f_{\mathrm{Pd}} = (156 \pm 18)\,\%$ and $f_{\mathrm{Y}} = (112 \pm 3)\,\%$.

Transmission measurements on Pd01 revealed, that even a small layer of palladium

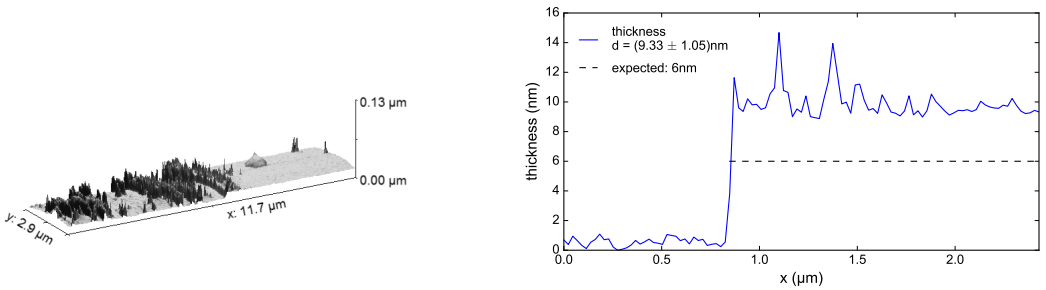

(a) **(b)**

Figure 4.8: AFM measurements on Pd01. **(a)** shows film topography. Material builds up when part of the film is scratched away, leaving a very irregular surface (left). **(b)** is the thickness profile used to estimate film thickness.

significantly lowers the transmittance across all wavelengths (fig. 4.9). As only the yttrium layer in the Y/Pd system changes its optical properties when exposed to hydrogen (fig. 4.9), its impact on the transmittance depends significantly on the thickness of the

palladium layer. A thinner palladium film will increase the effect the phase transition has on the combined spectrum, while it will also make the yttrium layer more prone to oxidation. Fourier transform infrared spectroscopy for F02 reveals that the spectrum shift

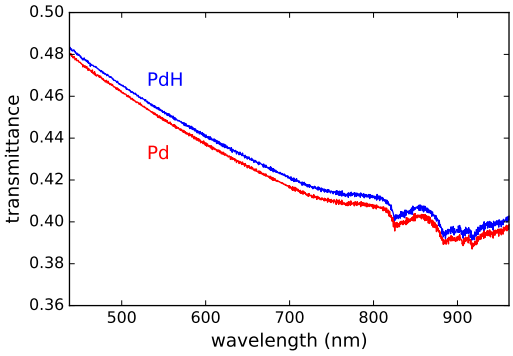

Figure 4.9: Transmittance spectra for Pd01 before (red), and after hydrogenation (blue). No significant shift could be observed.

can be observed well into the infrared region (fig. 4.10a), in fact, the infrared regime is where the phase transition will have the largest impact on the optical properties (compare dielectric functions for YH_2 and YH_3 in fig. 2.8d and fig. 2.8f). For both measurements, transmittance in the visible, and reflectance in the infrared regime, no transmittance shift for the transition from Pd to PdH could be observed for the Pd01 sample.

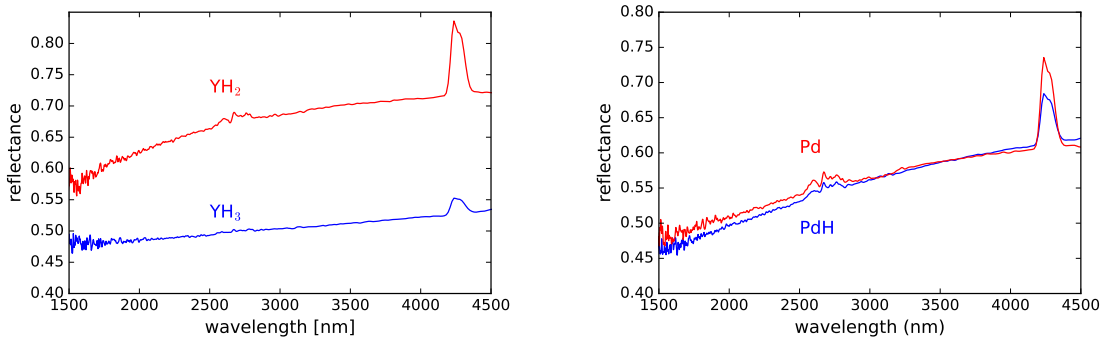

(a) **(b)**

Figure 4.10: FTIR measurements before (red) and after (blue) hydrogen loading. **(a)** shows the reflectance for sample F02, as YH_2 is less transparent, a higher reflectance is expected. **(b)** is the reflectance measured on a Pd01, where no change between Pd and PdH phases could be observed. A gold mirror was used as a reference for both measurements.

4.2.3 F03 - Variation of Cover Layer

To investigate different cover layer thicknesses, a film with a 50 nm thick yttrium layer covered by 3 nm of palladium was produced (evaporation data see tab. 4.4). Initial

	yttrium	palladium
rate (Å/s)	0.24 - 0.26	0.06
pressure range (10^{-8} mbar)	4.2 - 10.0	1.7 - 1.9
duration (min)	33.55	8.2
expected thickness (nm)	50.0	3.0

Table 4.4: Evaporation parameters for F03.

hydrogenation with 5 vol% hydrogen exposure is shown in fig. 4.11a. Compared to F02, the F03 sample reaches a higher final transmittance ($T(700\,\text{nm}) = 0.40$ vs. $T(700\,\text{nm}) = 0.29$ for the YH_3 phase respectively). This can be attributed to the thinner palladium cover layer. Repeated hydrogen loading and unloading (see fig. 4.11b) revealed that the $YH_3 \longrightarrow YH_2$ transition was really slow for F03, as the sample never fully transitioned back into the YH_2 phase, where it had started out (transmittance before the first cycle: $T(700\,\text{nm}) = 0.36$, as opposed to $T(700\,\text{nm}) = 0.39$ after the first cycle). As the initial hydrogenation $Y \longrightarrow YH_2 \longrightarrow YH_3$ was successful for F03 (fig. 4.11a), the smaller cover layer may have caused the sample to degrade much faster than F02, where repeated cycles showed only minor degradation over time. While at the start the yttrium had not yet oxidized, over time an Y_2O_3 layer started to form, hindering hydrogen diffusion. Investigations of film thickness for F03 using AFM (see fig. 4.12) reveals a much thicker

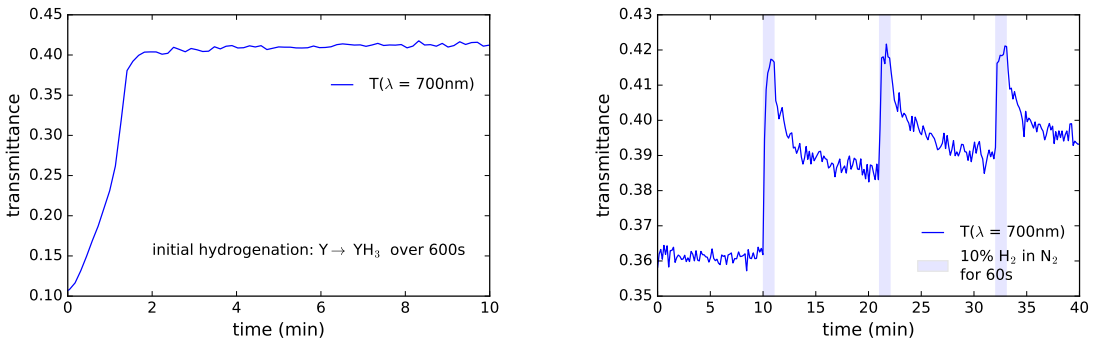

(a) **(b)**

Figure 4.11: Time traces of the transmittance for $\lambda = 700\,\text{nm}$. **(a)** shows the transmittance change during initial exposure to hydrogen when the Y to YH_3 transition occurs. **(b)** shows the transmittance during repeated hydrogen loading and unloading.

film than expected, even thicker than F02. This confirms that estimating layer thickness through monitoring deposition rate and evaporation time is not perfectly reliable, making investigations of different cover layer thicknesses difficult, as the exact thickness cannot be predicted.

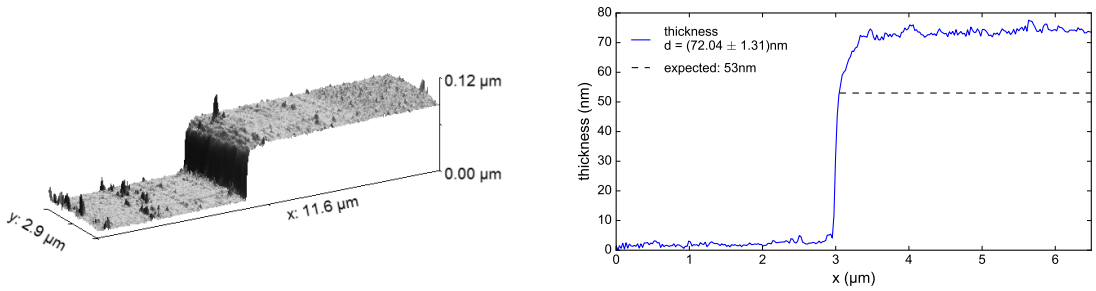

(a) **(b)**

Figure 4.12: AFM measurements on F03. **(a)** shows the measured topography. **(b)** is the thickness profile used to estimate film thickness.

4.2.4 F04 - 2nd Optimization

Sample F04 was produced using results from experiments on F02. Evaporation parameters are shown in table 4.5. For F04, besides using the determined tooling factors to correct for layer thickness, higher deposition rates were used, reducing deposition time and therefor exposure to residual gases, reducing the exposure of the yttrium layer to oxygen.

	yttrium	palladium
rate (Å/s)	0.330	0.285
pressure range (10^{-8} mbar)	3.6 - 5.9	1.4 - 1.9
duration (min)	24.5	3.5
expected thickness (nm)	50.1	6.0

Table 4.5: Evaporation parameters for F04.

Initial hydrogenation (5 vol% hydrogen exposure) shows a drastic change in transmittance as the yttrium transforms to its dihydride (YH_2) and eventually trihydride (YH_3) phase (fig. 4.13a). After the transmittance initially increases linearly with time for about 24 s, a switch to an exponential dependency can be observed, suggesting that different YH_x phases have different hydrogen loading capabilities. This can be further confirmed by the time trace shown in fig. 4.13b, where the lower limit of transmittance is measured to be around $T_{min} = 0.23$ which is associated with the YH_2 phase and matches the transmittance

for initial hydrogen loading after 24 s. Unlike sample F02, no degradation of the switching contrast for continuous hydrogen loading and unloading (fig. 4.13b) can be observed for F04, with switching times of about 108 s for the transition from YH_2 to YH_3, and 693 s when transitioning from YH_3 to YH_2. The time development of the transmission spectrum

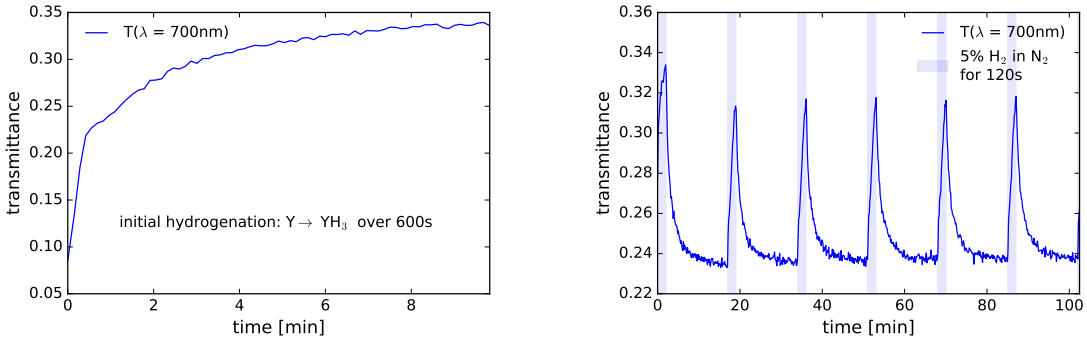

(a) **(b)**

Figure 4.13: Time traces of the transmittance for $\lambda = 700\,\text{nm}$. **(a)** shows the transmittance change during initial exposure to hydrogen, a change in dynamics is observed after 24 s where the transition from Y $\longrightarrow$ YH_2 has finished and YH_2 $\longrightarrow$ YH_3 begins. **(b)** shows the transmittance during repeated hydrogen loading and unloading. No degradation is observed after several cycles.

for hydrogen loading and unloading is shown in fig. 4.14. A clear difference in shape is observable when comparing the spectra for the two phases, suggesting that the refractive index changes its wavelength dependency. The dielectric function for YH_2 is negative for wavelengths $\lambda < 500\,\text{nm}$ and $\lambda > 800\,\text{nm}$ (see fig. 2.8d) which is in line with what is observed in fig. 4.14 as the change in transmittance is most pronounced in these regions.

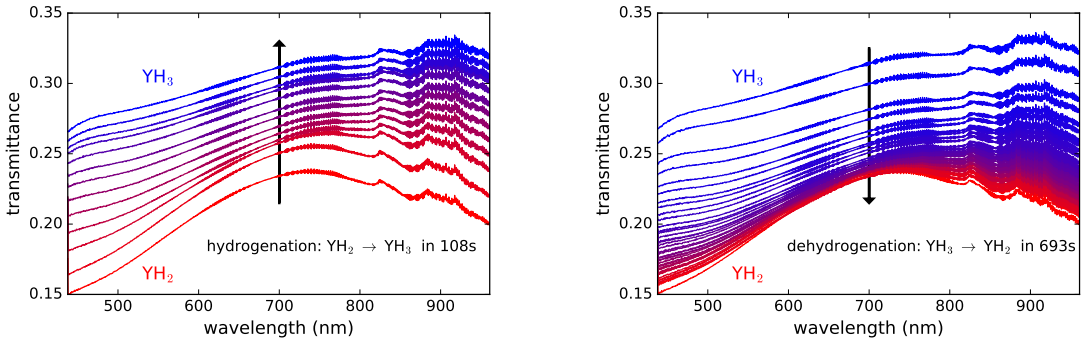

(a) **(b)**

Figure 4.14: Transmittance shift over time for sample F04. **(a)** shows the shift during hydrogen loading, **(b)** during unloading.

To determine how well the palladium cover layer protects the yttrium from oxidation, the change in transmittance over time for $\lambda = 700\,\text{nm}$ during hydrogen exposure was measured, once right after sample preparation and once again a week later. The sample was stored in a vacuum in between measurements. Results are shown in fig. 4.15. Even though the sample had been stored in a vacuum, keeping oxygen exposure to a minimum, it no longer responds to the hydrogen exposure, even at higher concentration. This suggest that the palladium layer does not prevent the oxidation of the yttrium film entirely, some degradation over time is expected. Thicker cover layers may work against this problem, prolonging the lifetime of the yttrium layer.

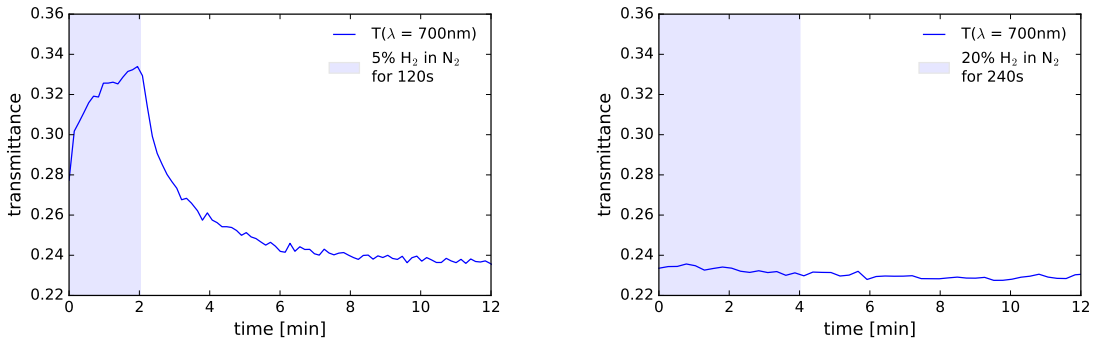

(a) **(b)**

Figure 4.15: Degradation measurement. **(a)** shows the transmittance for $\lambda = 700\,\text{nm}$ during hydrogen loading, measured right after the sample was fabricated. **(b)** is the same measurement (using higher hydrogen concentration as well as a longer exposure) after the sample had been stored in vacuum for a week, showing that the sample has ceased to respond to hydrogen exposure.

4.2.5 F05 - Reproducibility

As a final step a fifth film (F05) was produced to check whether the results from F04 could be reproduced. Evaporation data is shown in tab. 4.6. The transmittance spectra

	yttrium	palladium
rate (Å/s)	0.367	0.295
pressure range (10^{-8} mbar)	4.4 - 8.9	3.0 - 3.8
duration (min)	22.7	3.4
expected thickness (nm)	50.0	6.0

Table 4.6: Evaporation parameters for F05.

for both samples (F04 and F05) and all three phases (Y, YH_2 and YH_3) are compared

in fig. 4.16a. The spectra agree well with each other, confirming reproducibility of the optimized deposition process. The YH_3 phase for F05 is slightly more transparent, which suggests that F05 has higher hydrogen loading capabilities than F04.

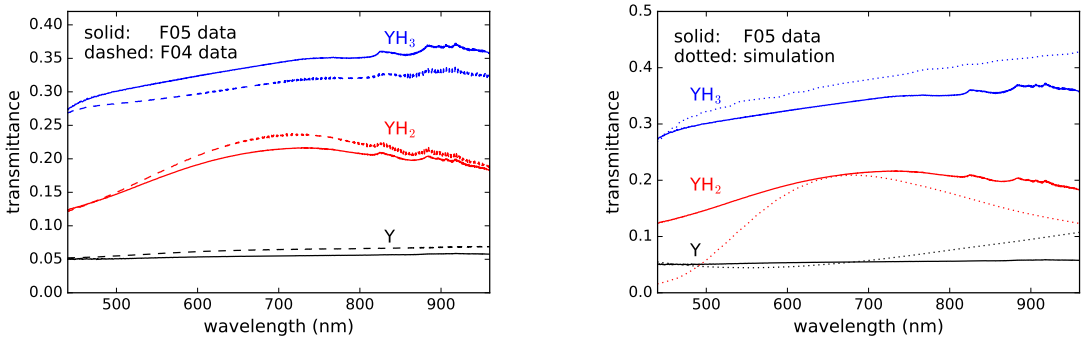

Figure 4.16: Comparisons **(a)** between samples F04 and F05; **(b)** between sample F05 and simulated data.

Figure 4.16b shows comparisons of the transmittance spectra for the YH_2 and YH_3 phases with simulations. YH_2 simulations are on a 50 nm thick YH_2 film with 6 nm palladium on top. For the YH_3 phase, a 50 nm thick YH_3 film with 6 nm PdH on top was used.

A general agreement between the simulations and experimental data is observed. Simulations for the YH_3 phase show a slightly higher transmittance across all wavelengths, suggesting that not the entire yttrium layer transitioned into the trihydride phase. A similar observation is made regarding the YH_2 phase, where for both ends of the spectrum a higher transmittance is measured compared to the simulation. Both observations suggest that the film does not switch between the YH_2 and YH_3 phases in the observed timescales but rather between two intermediate phases YH_x and YH_y with $2 < x < y < 3$.

5 Summary, Discussion, and Outlook

The evaporation of yttrium and palladium was investigated in order to produce thin yttrium films covered by palladium, that exhibit the hydrogen induced metal-insulator phase transition.
Samples were produced by depositing an yttrium film onto SiO_2 substrates with an ITO layer on top, then evaporating a thin palladium layer as protection.
For each sample the change in optical properties when undergoing phase transition was examined using transmission spectroscopy and Fourier-transform infrared spectroscopy. Film thickness was investigated using atomic force microscopy. Samples were produced by depositing an yttrium film onto SiO_2 substrates with an ITO layer on top, then evaporating a thin palladium layer to prevent oxidation and catalyse hydrogen diffusion.

The first sample F01 already exhibited the desired phase transition. A transmittance shift across all wavelengths could be observed once the sample was exposed to hydrogen causing the $Y \longrightarrow YH_2 \longrightarrow YH_3$ transition, while the irreversibility of $Y \longrightarrow YH_2$ could also be confirmed.
Improving on evaporation parameters by lowering ambient pressure and stabilizing deposition rates proved to be beneficial to film characteristics, as confirmed with sample F02. A time trace of the transmittance revealed that the $Y \longrightarrow YH_2$ transition, although irreversible, happens much faster than the reversible $YH_2 \longrightarrow YH_3$ transition.
Measurements of the transmittance for several cycles of hydrogen loading and unloading revealed possible switching times of 41 s for $YH_2 \longrightarrow YH_3$ (which still can be improved upon by using higher hydrogen concentrations) and 470 s for $YH_3 \longrightarrow YH_2$. A limiting factor for the switching times is the diffusion through the yttrium layer into the palladium layer. The formation of an Y_2O_3 layer over time hinders the diffusion, and causes switching speeds, and contrast, to degrade. This theory is confirmed through measurements on F03, which featured a thinner palladium cover layer. This sample showed significant degradation, which can be attributed to the thinner cover layer, making it more prone to oxidize.
Measurements on a palladium film to investigate the influence of the cover layer on the transmittance revealed that the palladium has a significant impact on the overall transmittance, decreasing the transmittance by up to 60 % (9 nm thick palladium layer). Using

thinner palladium cover layers would increase the effect the yttrium phase transition has on the overall spectrum, however, this would also make the film more prone to degradation.

When the palladium film Pd01 was exposed to hydrogen, no transmittance shift could be observed, confirming that it is the yttrium phase transition that is responsible for shifting the transmittance.

AFM measurements revealed that film thickness was a parameter difficult to control with the setup. Before investigations into the effect of different cover layer thicknesses can begin, a solution to this problem would have to be developed. A starting point would be, to more accurately determine the tooling factors for each source material by depositing yttrium and palladium seperately, and then using atomic force microscopy to determine the actual thickness.

FTIR measurements revealed that the effect the yttrium phase transition has on the optical properties extends well into the infrared region, where the difference between the YH_2 and YH_3 is even greater. Fabricating nanodevices that operate in this region is especially interesting, as demonstrated by Strohfeldt et al. in [18]

As has been shown with F04, which exhibits a 40 % higher switching contrast for $\lambda = 700\,\text{nm}$ compared to F02, increasing the deposition rate yields better results. However, the setup used for evaporation is limited regarding evaporation rate, as crucible size and heating power are both limited. Further studies, using higher deposition rates, would have to be conducted using a different setup.

The reproducibility of the results from F04 has been proven through measurements on F05, showing almost identical optical properties. Simulations are in good agreement with the optical characteristics observed. Deviations from the simulated data are mostly for the YH_2 phase, suggesting that at the time of the measurements, the samples had not fully transitioned back into the YH_2 phase. This relates closely with the observed degradation effects.

Going forward, the effect of a titanium adhesion layer would have to be investigated as an intermediate step towards the fabrication of yttrium nanostructures.

Nanostructures that featuring yttrium as an active component, would be controllable just like the samples in this work, using hydrogen as an external stimulus. Taking advantage of the metal-insulator phase transition of yttrium, resonances could be switched on (metallic phase, YH_2) and off (dielectric phase, YH_3) creating new ways of interacting with nanomaterials.

6 References

[1] C. B. Alcock, V. P. Itkin, and M. K. Horrigan. "Vapour Pressure Equations for the Metallic Elements: 298-2500K". In: *Canadian Metallurgical Quarterly* 23.3 (1984), pp. 309–313. DOI: 10.1179/cmq.1984.23.3.309. URL: https://doi.org/10.1179/cmq.1984.23.3.309.

[2] Kurt. J. Lesker Company. *Material Deposition Chart*. https://www.lesker.com/newweb/deposition_materials/materialdepositionchart.cfm?pgid=0.

[3] M. Gartz and M. Quinten. "Broadening of resonances in yttrium nanoparticle optical spectra". In: *Applied Physics B: Lasers and Optics* (2001). ISSN: 09462171. DOI: 10.1007/s003400100702.

[4] FOCUS GmbH. *EFM Evaporators*. Brochure. 2017. URL: http://www.focus-gmbh.com/uhv-instruments/EFM/styled-5/EFM.html.

[5] A.T.M. van Gogh et al. "Structural, electrical, and optical properties of La1-zYzHx switchable mirrors". In: *Physical Review B* (2001). ISSN: 0163-1829. DOI: 10.1103/PhysRevB.63.195105.

[6] Saulius Grazulis et al. "Crystallography Open Database (COD): an open-access collection of crystal structures and platform for world-wide collaboration". In: *Nucleic Acids Research* 40.D1 (2012), pp. D420–D427. DOI: 10.1093/nar/gkr900. eprint: http://nar.oxfordjournals.org/content/40/D1/D420.full.pdf+html. URL: http://nar.oxfordjournals.org/content/40/D1/D420.abstract.

[7] J.N. Huiberts et al. "Yttrium and lanthanum hydride films with switchable optical properties". In: *Nature* 380 (1997). URL: https://www.nature.com/articles/380231a0.pdf.

[8] *Introduction to Polarization — Edmund Optics*. https://www.edmundoptics.de/resources/application-notes/optics/introduction-to-polarization/. (Accessed on 08/05/2018).

[9] Stefan Alexander Maier. *Plasmonics: Fundamentals and Applications* -. Berlin Heidelberg: Springer Science & Business Media, 2007. ISBN: 978-0-387-37825-1.

[10] Milton Ohring. *Materials science of thin films. deposition and structure*. eng. 2nd ed. San Diego, CA: Academic Press, 2002, Online–Ressource (1 v. p.) ISBN: 978-0-08-049178-3. URL: http://proquest.tech.safaribooksonline.de/9780125249751.

[11] OverlordQ. *Atomic force microscope block diagram.* [Online; accessed July 31, 2018]. 2008. URL: https://commons.wikimedia.org/wiki/File:Atomic_force_microscope_block_diagram.svg.

[12] Ana Maria Racu. *Micro-Raman spectroscopy study of ordering phenomena in YHx thin films and in CuTe2O5 single crystals.* Cuvillier, 2005. ISBN: 9783865375674.

[13] Remhof and Arndt. "Hydrogen in Yttrium Films Structure and Phase Formation Arndt Remhof". In: (2000). URL: http://www-brs.ub.ruhr-uni-bochum.de/netahtml/HSS/Diss/RemhofArndt/diss.pdf.

[14] Jafar Safarian and Thorvald A Engh. "Vacuum Evaporation of Pure Metals". In: (). DOI: 10.1007/s11661-012-1464-2. URL: https://link.springer.com/content/pdf/10.1007%7B%5C%%7D2Fs11661-012-1464-2.pdf.

[15] Constantin Schuster. "Darkfield Microscopy on plasmonic Nanostructures". Bachelor's Thesis. Heidelberg University, 2018.

[16] Olaf Stenzel. *The Physics of Thin Film Optical Spectra - An Introduction.* Berlin, Heidelberg: Springer, 2015. ISBN: 978-3-319-21602-7.

[17] Florian Sterl et al. "Magnesium as Novel Material for Active Plasmonics in the Visible Wavelength Range". In: *Nano Letters* 15.12 (2015). PMID: 26312401, pp. 7949–7955. DOI: 10.1021/acs.nanolett.5b03029. eprint: https://doi.org/10.1021/acs.nanolett.5b03029. URL: https://doi.org/10.1021/acs.nanolett.5b03029.

[18] Nikolai Strohfeldt et al. "Yttrium Hydride Nanoantennas for Active Plasmonics". In: *Nano Letters* 14.3 (), pp. 1140–1147. DOI: 10.1021/nl403643v. URL: https://pubs.acs.org/doi/pdf/10.1021/nl403643v.

[19] Stanford Research Systems. *QCM100 - Quartz Crystal Microbalance Theory and Calibration.*

[20] T.J. Udovic, Q. Huang, and J.J. Rush. "Characterization of the structure of YD3 by neutron powder diffraction". In: *Journal of Physics and Chemistry of Solids* 57.4 (1996), pp. 423–435. ISSN: 0022-3697. DOI: https://doi.org/10.1016/0022-3697(95)00254-5. URL: http://www.sciencedirect.com/science/article/pii/0022369795002545.

[21] P. Vajda. "Chapter 137 Hydrogen in rare-earth metals, including RH2+x phases". In: vol. 20. Handbook on the Physics and Chemistry of Rare Earths. Elsevier, 1995, pp. 207–291. DOI: https://doi.org/10.1016/S0168-1273(05)80071-6. URL: http://www.sciencedirect.com/science/article/pii/S0168127305800716.

Acknowledgements

I would like to thank Prof. Dr. Laura Na Liu for allowing me to be part of her work group and making this thesis possible.
Prof. Dr. Yana Vaynzof for the co-examination.
Dr. Frank Neubrech for his supervision and helpful tips along the way.
Prof. Dr. Annemarie Pucci for allowing me to use her laboratories, as well as Dr. Christian Huck and Michael Tzschoppe for introducing me into the experimental setups and their advice regarding thin film deposition.
Constantin Schuster for setting up the transmission microscope as well as conducting the measurements and
Anton Kompatscher, who assisted with the evaporator setup and provided simulations for the different films.

Erklärung

Ich versichere, dass ich diese Arbeit selbstständig verfasst und keine anderen als die angegebenen Quellen und Hilfsmittel benutzt habe.

Ort,Datum	Felix Scherz